J Mater Sci (2008) 43:1480–1485
DOI 10.1007/s10853-007-2331-1

A study of microstructure and phase constitutions of the Cr–Ni surfacing layers deposited on Fe_3Al intermetallic by SMAW

Haijun Ma · Yajiang Li · S. A. Gerasimov · Juan Wang

Received: 18 March 2007 / Accepted: 19 November 2007 / Published online: 12 December 2007

Abstract Three different Cr–Ni alloys were deposited on the surface of Fe_3Al intermetallic by shielded metal arc welding (SMAW) to investigate the weldability of this material. The microstructure, phase constitutions, and fine structures of Cr–Ni surfacing layers were analyzed via metalloscope, SEM, XRD, and TEM. The results indicated that the Fe_3Al/Cr–Ni joint shows no cracks when Cr25–Ni13 alloy was deposited. The surfacing layer consisted of austenite (A), pro-eutectoid ferrite (PF), carbide-free bainite (CFB), lath martensite (LM), and little acicular ferrite (AF). Phase constitutions of the joint included Fe_3Al, FeAl, γ-(Fe,C), γ-(Fe,Ni), NiAl, and Ni_3Al. The lattice orientation for CFB between α *and* γ phases was $(110)_\alpha//(111)_\gamma$. Typical LM was composed of interlayer-carbide and α ferrite of 400 nm in length and 40 nm in width.

Introduction

Fe_3Al intermetallic exhibits excellent resistance to oxidation and corrosion, as well as creep resistance at high temperature, low density, and low raw material cost. It is hoped to be a new type of structural material in the aviation, petroleum, and power industries [1–4]. However, Fe_3Al is very brittle and sensitive to hydrogen brittleness to suffer cold cracks during welding [5, 6]; in addition, the high linear expansion coefficient and low coefficient of thermal conductivity make it easier to produce larger residual stress to induce hot cracking [7, 8]. Therefore, solving the welding issue of Fe_3Al is the key to promote its application. Fe_3Al intermetallic was successfully bonded by means of vacuum diffusion bonding [9], electronic beam welding, and plasma welding. But the costly equipments, complex technologies, and the size restriction to the workpiece impede the commercial application of these welding methods for Fe_3Al.

Some researchers deposited Fe_3Al intermetallic on the stainless steel surface after 500 °C pre-heating the matrix and 700 °C postweld heat treatment [10]. However, it would be extremely significant to accelerate its application if the welding for Fe_3Al via common welding technique at room temperature can be achieved. Therefore, the welding materials must be selected correctly. In this article, Cr–Ni alloys series with excellent anti-crack performance were used as the welding materials to investigate the technological weldability of Fe_3Al. The microstructure, micro-phase constitutions, and fine structures of the surfacing layer were studied to determine optimum Cr–Ni alloy and suitable shielded metal arc welding (SMAW) parameters. And an untextured fusion zone with no cracks was expected. This will provide an important experimental and theoretical basis for accelerating the application of Fe_3Al intermetallic as the engineering materials.

Experimental

Materials used in the test were Fe_3Al intermetallic plates and a series of Cr–Ni alloy bars. Fe_3Al was melted by the

H. Ma (✉) · Y. Li · J. Wang
Key Lab of Liquid Structure and Heredity of Materials, Ministry of Education, Shandong University (South Campus), Jing Shi Road 73, Jinan 250061, Shandong, P.R. China
e-mail: hjma123@mail.sdu.edu.cn

Y. Li · S. A. Gerasimov
Material Science Department, Bauman Moscow State Technical University, Moscow 105005, Russia

Table 1 Compositions and thermo-physical properties of Fe_3Al intermetallic

Compositions (wt.%)								
Fe	Al	Cr	Nb	Zr	B	Mn	Ce	
81.02	16.82	0.78	0.63	0.28	0.01	0.1	0.15	
Thermo-physical properties								
Structure	Ordered critical temperature (°C)	Young's modulus (GPa)	Melting point (°C)	Coefficient of heat expansion (10^{-6}·K^{-1})	Density (g·cm^{-3})	Tensile strength (MPa)	Elongation (%)	Hardness HRC
DO_3	540	140	1,540	11.5	6.72	455	2	≥29

Table 2 Compositions and mechanical properties of Cr–Ni alloys

Alloy series	Compositions (wt.%)						Mechanical property / MPa	
	C	Cr	Ni	Mn	Mo	Si	σ_b	δ_5
Cr18–Ni8	≤0.08	18.0–21.0	9.0–11.0	0.5–2.5	≤0.75	≤0.90	≥550	≥35
Cr18–Ni13	≤0.08	17.0–20.0	11.0–14.0	0.5–2.5	2.0–3.0	≤0.90	≥520	≥30
Cr25–Ni13	≤0.15	22.0–25.0	12.0–14.0	0.5–2.5	≤0.75	≤0.90	≥550	≥25

vacuum induction furnace and then fabricated into plates by the hot rolled technology, whose compositions and thermo-physical properties were shown in Table 1. The compositions and mechanical properties of three Cr–Ni alloys were shown in Table 2.

The oxidation film and greasy dirt on the surfaces of Fe_3Al and Cr–Ni alloys were removed by mechanical and chemical methods before welding. Then, three Cr–Ni alloys were deposited separately by SMAW on the Fe_3Al surface at room temperature. The obtained Fe_3Al/Cr–Ni alloys joints were cut into the size of $10 \times 10 \times 8$ mm^3 via line cutting. The Master MLS2500 welder made in Norway was applied and the welding parameters were: welding current 80 A, arc voltage 20–22 V, welding speed 4.2–4.5 mm/s, feed rate of wire about 1.2 m/min, gas flow about 6 L/min.

The Fe_3Al/Cr–Ni alloys joints after grinding and polishing were prepared into metallographic samples and then etched by a solution including HCl and HNO_3 (3:1). The microstructure morphology of the Cr–Ni surfacing layers were analyzed by means of Nikon AFX-|| A metalloscope, JXA-840 scanning electron microscope (SEM), and H-800 transmission electron microscope (TEM). The microhardness distribution and phase constitutions were measured via microsclerometer and D/MAX-RC X-ray diffraction (XRD), respectively.

Results and discussion

Microstructure morphology of the Cr–Ni surfacing layers

When the Cr18–Ni8 and Cr18–Ni13 alloys were deposited, the surfacing alloys splashed severely during welding and the surfacing layers with bad appearance were formed. Obvious longitudinal and transverse cracks distributed in the fusion zone, see Fig. 1a. When the Cr25–Ni13 alloy was applied, there was little splash and an untextured fusion zone with no cracks was obtained, see Fig. 1b. And the fusion zone was composed of two microstructure layers. The white microstructure layer was formed near Fe_3A1 substrate and the dark one formed near surfacing layer. The Cr25–Ni13 surfacing layer near fusion zone consisted of coarse and directional austenite (A) owing to the larger heat-transfer rate.

When the Cr25–Ni13 alloy was applied, the single-phase primary δ ferrite first precipitated from the molten pool when solidified. And the phase transformations from primary δ ferrite to γ austenite, as well as from γ to ferrite (F), martensite (M), and bainite (B) had occurred continuously. The matrix of the surfacing layer at room temperature was austenite (A). Little retained δ ferrite, bainite (B), and martensite (M) distributed on the austenite grain boundaries or inside the grains, see Fig. 2.

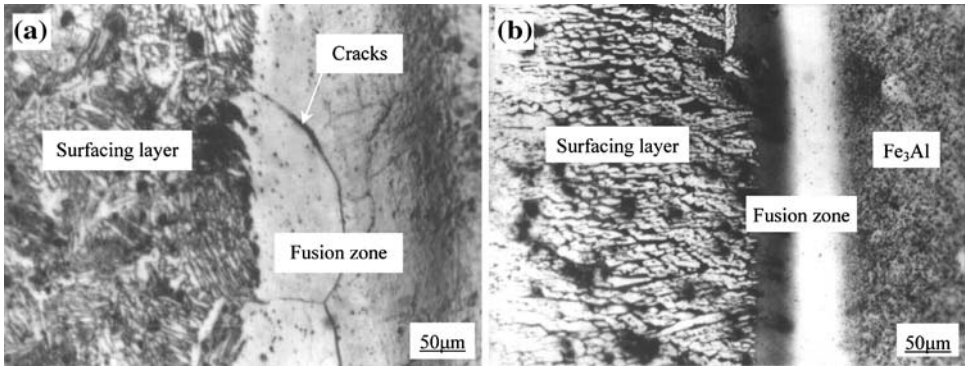

Fig. 1 Microstructure feature of the Cr–Ni alloy surfacing layers. (**a**) Cr18–Ni8 surfacing layer. (**b**) Cr25–Ni13 surfacing layer

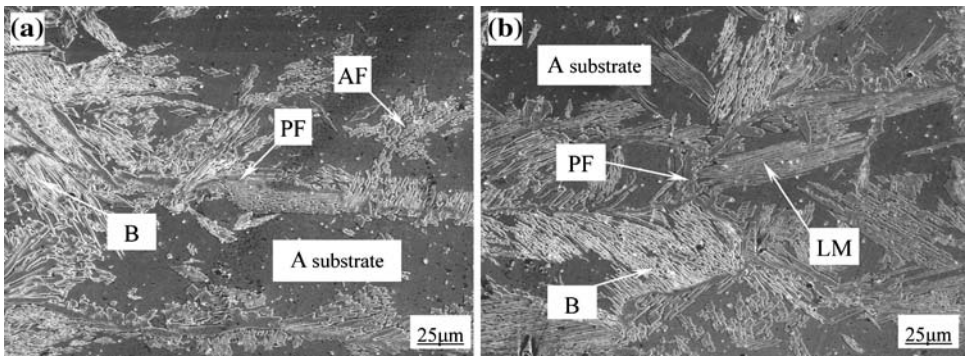

Fig. 2 Microstructure feature of the Cr25–Ni13 surfacing layer. (**a**) Cr25–Ni13 surfacing layer with more B. (**b**) Cr25–Ni13 surfacing layer with more LM

The microstructure in the middle Cr25–Ni13 surfacing layer was very complicated. Pro-eutectoid ferrite (PF) precipitated along the austenite (A) grain boundaries and formed the PF nets. Bainite (B) originated from the austenite (A) grain boundaries and extended parallel into austenite (A) interior. The bainite (B) was composed of PF plates and easy to occur in the alloys containing Si or Al. The Al concentration in the surfacing layer was increased due to the dilution effect of Fe_3A1 substrate, which facilitated the formation of the bainite (B). Little acicular ferrite (AF) and some lath martensites (LM) distributed inside some austenite (A) grains, see Fig. 2.

In some areas of the surfacing layer, there were more bainites (B) but less lath martensites (LM). The large quantity of white plates were the bainite (B) groups, see Fig. 2a. However, there were more lath martensites (LM) but less bainites (B) in other areas, see Fig. 2b. The quantity of the bainite (B) and lath martensite (LM) might be related to the cooling velocity and local Al concentration. Accordingly, there were more bainites (B) in the areas where Al concentration was higher or the cooling velocity was less, and more lath martensites (LM) in the areas with larger cooling velocity. The LM with higher strength, higher hardness, and good toughness was favorable in improving the mechanical performance of the surfacing layer.

Microhardness and phase constitutions near the Fe_3A1/Cr25–Ni13 joint

While a satisfactory deposit was achieved with Cr25–Ni13 alloy, the Cr25–Ni13 surface layer was further characterized by microhardness and phase constitutions. The microhardness was measured by means of SHIMADZU microsclerometer, with a test loading 100 g and a loading time 10 s. Microhardness distribution near the Fe_3A1/Cr25–Ni13 joint was shown in Fig. 3.

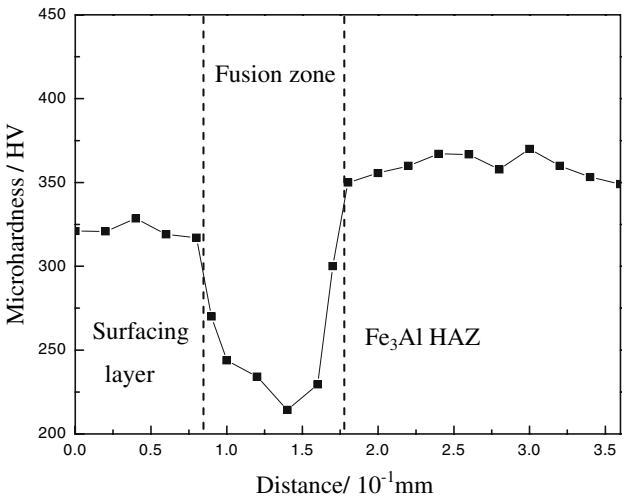

Fig. 3 Microhardness near the Fe_3A1/Cr25–Ni13 joint

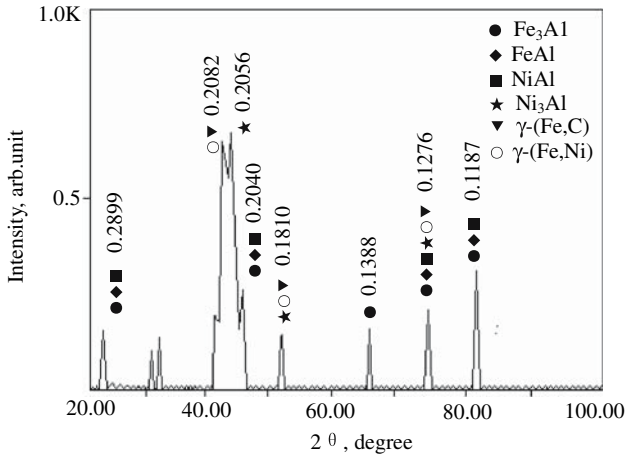

Fig. 4 XRD results near the Fe_3A1/Cr25–Ni13 joint

It was shown in Fig. 3 that the width of the fusion zone was about 0.1 mm, and the microhardness of the fusion zone was lower obviously than that of Fe_3A1 heat affected zone (HAZ) and Cr25–Ni13 surfacing layer. This microhardness distribution with center lower and "shoulders" higher can be regarded as lower-strength matched weld, which can ensure the ductility of the fusion zone to avoid welding cracks. The average microhardness of the fusion zone was about HV250 and the lowest was HV210.

From the Cr25–Ni13 surfacing layer side to the HAZ side across the fusion zone, the microhardness was first decreased and then increased, see Fig. 3. The microhardness of fusion zone near the Cr25–Ni13 surfacing layer was lower than that near the HAZ. Since the microhardness of fusion zone was lower, some lower-microhardness phases were likely to produce there. Considering the compositions of the applied materials, the lower-microhardness phases might be Ni–Al compounds which had better toughness. It was necessary to determine what exactly the Ni–Al compounds were.

The phase constitutions near the Fe_3A1/Cr25–Ni13 joint were further determined by means of D/MAX-RC X-ray diffraction (XRD). The XRD analysis was carried out with copper target under the following conditions: voltage 40 kV and current 40 mA. The XRD analysis results were shown in Fig. 4. The phase constitutions were very complicated. Except the basis Fe_3Al and γ-(Fe,C) phases corresponding to base material and surfacing layer respectively, there were also FeAl, NiAl, γ-(Fe,Ni), and Ni_3Al phases.

During the fusing process of Fe_3Al and Cr25–Ni13 alloy, Fe, Al, Cr, Ni elements diffused and mixed to induce a series of chemical reactions to produce some new phases. The FeAl compound was formed in the zone where the Al concentration was higher. The Ni–Al compounds, namely Ni_3Al and NiAl, were formed depending on the Ni and Al contents. Ni_3Al has excellent room-temperature toughness and lower microhardness. Corresponding to the microhardness distribution state near the Fe_3A1/Cr25–Ni13 joint, it was in the fusion zone where the Ni–Al compounds were formed. The existence of Ni_3Al was able to migrate the brittleness to ensure sufficient toughness of the fusion zone to avoid welding cracks. The formation of Ni_3Al was very important for Fe_3Al welding at room temperature. It provided a new way to improve the technological weldablity of Fe_3Al.

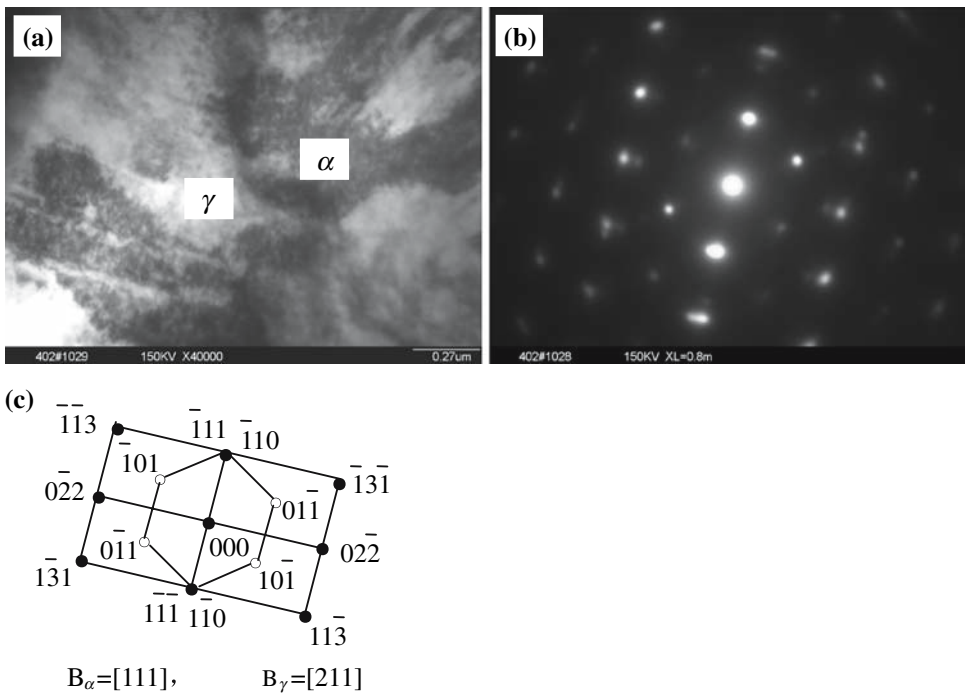

Fig. 5 Fine structure of carbide-free bainite (CFB). (**a**) TEM morphology. (**b**) Electron diffraction pattern. (**c**) Schematic index diagram

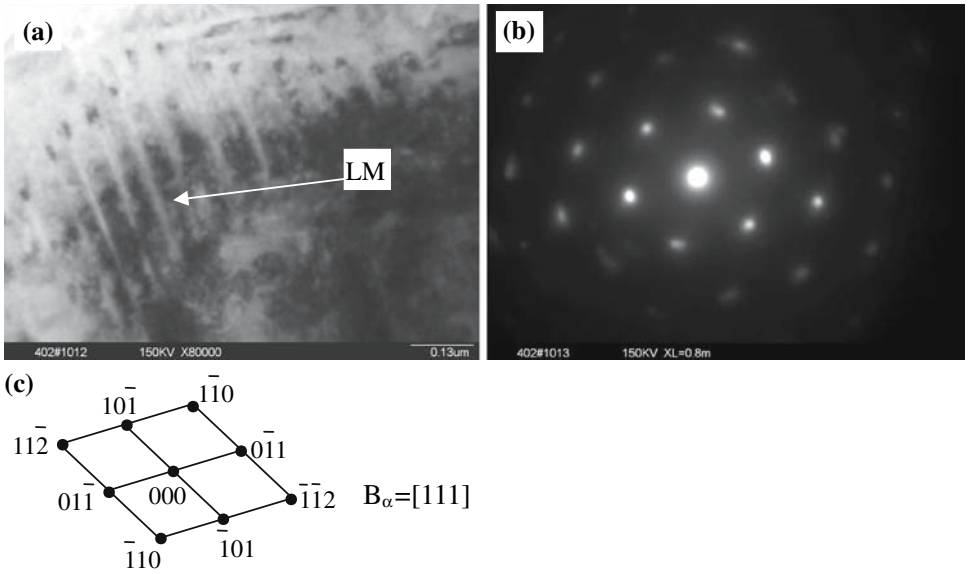

Fig. 6 Fine structure of lath martensite (LM). (**a**) TEM morphology. (**b**) Electron diffraction pattern. (**c**) Schematic index diagram

TEM analysis of the Cr25–Ni13 surfacing layer

To clarify further the fine structure of the constituent phases, some thin foils cut from the Cr25–Ni13 surfacing layer were analyzed by TEM and electron diffraction. TEM morphology, electron diffraction pattern and index schematic diagram were shown in Figs. 5 and 6.

It can be seen in Fig. 5 that there were a large number of dislocations inside α phase, thus dislocation group was formed. Conversely, there was little dislocation in γ phase. Fig. 5c showed the composite index diagram of electron diffraction pattern for α and γ phases. The selected zone axis were $B_\alpha = [111]$ and $B_\gamma = [211]$. The lattice orientation between α and γ phases was $(110)_\alpha // (111)_\gamma$, corresponding to special orientation relation N-W. Accordingly, the phases selected for electron diffraction pattern were carbide-free bainite (CFB), as seen in Fig. 2. α phase nucleation and grew up along certain habit-plain of γ phase of $\{111\}_\gamma$. These phases were composed of sub-crystal structure without any obvious brittle phases and micro-defects such as pore and cracks.

Figure 6 showed the TEM morphology and corresponding electron diffraction pattern of typical LM. The selected zone axis was $B_\alpha = [111]$. The black zonal structure in parallel arrangement with 400 nm in length and 40 nm in width was α ferrite. And the white interlayers among α ferrite were carbide segregation. α ferrite and interlayer-carbide constituted LM. The existence of LM characterized by excellent mechanical property can improve the cracking resistance of the Fe_3A1/Cr25–Ni13 joint.

Conclusions

(1) When the Cr25–Ni13 alloy was used as surfacing material, the Fe_3A1/Cr25–Ni13 joint showed no cracks and fine microstructure was obtained. The fusion zone seemed to form two different microstructure layers. The parameters of SMAW were: welding at room temperature, welding current 80 A, arc voltage 20–22 V, welding speed 4.2–4.5 mm/s, feed rate of wire about 1.2 m/min, gas flow about 6 L/min.

(2) The Cr25–Ni13 surfacing layer was composed of austenite (A) matrix, pro-eutectoid ferrite (PF), carbide-free bainite (CFB), lath martensite (LM), and little acicular ferrite (AF). The quantity of B and LM was related to the cooling velocity and alloying elements concentration. The lattice orientation for CFB was $(110)_\alpha // (111)_\gamma$. Typical LM was composed of interlayer-carbide and α ferrite of 400 nm in length and 40 nm in width. The LM was favorable in improving cracking-resistance of the Fe_3A1/Cr25–Ni13 joint.

(3) The mixture and diffusion of Fe, Al, Cr, Ni elements during welding process produced some new phases, including FeAl, NiAl, γ-(Fe,Ni), and Ni_3Al except Fe_3Al and γ-(Fe,C) basis phases. Ni_3Al formed in the fusion zone was able to reduce the brittleness and ensure given toughness and lower microhardnes of the fusion zone to prevent welding cracks.

Acknowledgements This project was sponsored by the National Natural Science Foundation of China (50375088) and Doctoral Foundation of Shandong Province (2006BS04004) and Development project of Science and Technology of Shandong Province (2007GG10004016).

References

1. Fair GH, Wood JV (1994) J Mater Sci 29:1935. doi:10.1007/BF00351317
2. Mckamey CG, Devan JH, Tortorelli PE, Sikka VK (1991) J Mater Res 6:1779

3. Sikka VK, Wilkening D, Liebetrau J, Mackey B (1998) Mater Sci Eng 258A:249
4. Nachman JF, Buehler WJ (1974) Corrosion 30:357
5. Moret M, Jongenburger CP, Zhang L (1994) Scripta Metall Mater 31:1135
6. Castagna A, Stoloff NS (1995) Mater Sci Eng 192/193A:399
7. Mckamey CG, Maziasz PJ (1998) Intermetallics 6:303
8. David SA, Zacharia T (1993) Weld J 72:201
9. Li YJ, Wu HQ, Wang J (2003) Mater Sci Tech 19:227
10. Min XG, Yu XQ, Sun YS, Pang HX (2001) Trans China Weld Inst 22:56